

## Masses and Distance of the Young Binary NTTS 045251+3016

M. Simon<sup>1</sup>, G. H. Schaefer<sup>2</sup>, L. Prato<sup>3</sup>, Dary Ruíz-Rodríguez<sup>3</sup>, N. Karnath<sup>3</sup>, O. G. Franz<sup>3</sup>,  
and L. H. Wasserman<sup>3</sup>

Received \_\_\_\_\_; accepted \_\_\_\_\_

---

<sup>1</sup>Department of Physics and Astronomy, Stony Brook University, Stony Brook, NY 11794-3800, USA [michal.simon@stonybrook.edu](mailto:michal.simon@stonybrook.edu)

<sup>2</sup>The CHARA Array of Georgia State University, Mount Wilson Observatory, Mount Wilson, CA 91023, USA

<sup>3</sup>Lowell Observatory, 1400 West Mars Hill Rd., Flagstaff, AZ 86001, USA

## ABSTRACT

As part of our continuing campaign to measure the masses of pre-main sequence (PMS) stars dynamically and thus to assess the reliability of the discrepant theoretical calculations of contraction to the main sequence, we present new results for NTTS 045251+3016, a visual and double-lined spectroscopic binary in the Taurus-Star Forming Region (SFR). We obtained new high angular resolution astrometry and high spectral resolution spectroscopy at Keck Observatory. The new data lead to a significant revision of previously published orbital parameters. In particular, we find that the masses of the primary and secondary are  $0.86 \pm 0.11$  and  $0.55 \pm 0.05 M_{\odot}$ , respectively, smaller than previously reported, and that the system lies  $158.7 \pm 3.9$  pc from the sun, further than previously reported.

*Subject headings:* binaries: visual -stars: Pre-Main Sequence— stars: fundamental parameters—stars: individual (NTTS 045251+3016)

## 1. Introduction

The mass and age of a pre-main sequence (PMS) star are usually estimated by its location in the H-R diagram (HRD) relative to theoretical calculations of PMS evolution. Unfortunately, for stars less massive than  $\sim 1.5 M_{\odot}$ , these estimates vary depending on the calculations used (e.g., Simon 2008; Hillenbrand & White 2004). For example, for an M0 spectral type star younger than  $\sim 10$  Myr with luminosity  $L=0.5 L_{\odot}$ , the tracks can yield masses discrepant by a few tenths of a solar mass and ages discrepant by factors of 2 to 3. Dynamical techniques provide the only absolutely trustworthy measurements of mass and thus the only means to connect the theoretical calculations with reliable empirical input. We are pursuing a program to measure PMS stellar masses dynamically (e.g., Schaefer et al. 2012 and references therein) with sufficient precision and accuracy to identify a reliable set of evolutionary tracks for observers and to identify improvements that may be necessary to implement for theorists.

Walter et al. (1988) identified NTTS 045251+3016 (V397 Aur, TAP 57, HBC 427) as a single-lined pre-main sequence (PMS) binary in the Taurus-Auriga star forming region (SFR) on the basis of its visible light spectroscopy and X-ray emission. Steffen et al. (2001) resolved the binary using the *Fine Guidance Sensors* (FGS) of the *Hubble Space Telescope* and combined the results with visible light spectroscopy spanning 14 years and infrared (IR) spectroscopic measurements that detected the secondary. They derived the orbital parameters of the system as a visual binary (VB) and double-lined spectroscopic binary (SB2). In particular, Steffen et al. reported masses of the components, orbital period, semi-major axis, inclination, and the distance to the binary. These parameters were derived from astrometry covering about half the 6.9 year orbit, single-lined radial velocities (RVs) of the primary covering the full period, and only two IR spectroscopic measurements of both component RVs close together in phase but fortuitously at maximum RV separation. As a

result, the precisions of the primary and secondary masses are 13% and 11%, respectively, insufficient to discriminate definitively among theoretical calculations of PMS evolution (e.g., Simon et al. 2000). We therefore included NTTS 045251+3016 in our current program.

It is now possible to achieve angular resolution from the ground that is comparable to or exceeds that of the *FGS*. We present such results here. §2 describes our new observations obtained using adaptive optics (AO), non-redundant masking (NRM), two-telescope interferometry (archival data), and high resolution spectroscopy, all in the near-IR. To our surprise, we found that the new astrometry is inconsistent with Steffen et al.’s. §3 discusses this discrepancy, presents revised orbital parameters of the binary including new values for the component masses and distance, and compares the masses with theoretical calculations of PMS evolution. §4 summarizes our results.

## 2. Observations and Data Reduction

All of our observations (Table 1) were obtained with facility instrumentation at the two telescopes of the W.M. Keck Observatory. We describe the observations and their reduction in this section.

### 2.1. Two-telescope Interferometry

NTTS 045251+3016 was observed on seven nights with the two telescopes of the Keck Observatory operating as an IR interferometer (Colavita et al. 2004; Wizinowich et al. 2004). This mode was decommissioned in 2012. All Keck Interferometer (KI) data are now in the public domain; we obtained the data for NTTS 045251+3016 from the archives maintained at the *NASA Exoplanet Science Institute* (NExScI) at the California Institute

of Technology. The observations were originally proposed and planned by A. Sargent and A. Boden and were carried out by the KI observing staff.

Operating in its visibility-amplitude mode, the KI measured the visibility, or fringe contrast, of the target. The normalized visibility,  $V^2$ , of a binary when the diameter of each component is unresolved, a safe assumption for stars at the 140 pc distance of the Taurus SFR (Kenyon et al. 1994), is

$$V^2 = \frac{1 + r^2 + 2r \cos(2\pi \mathbf{B} \cdot \mathbf{s}/\lambda)}{(1 + r)^2} \quad (1)$$

where  $\lambda$  is the wavelength of observation, and  $r$ , the flux ratio of the components (e.g., Boden 2000; Berger & Segransan 2007). The projection of the binary separation vector  $\mathbf{s}$  on the interferometer baseline  $\mathbf{B}$  is given by  $(\mathbf{B} \cdot \mathbf{s})$ . The 85-m baseline of the KI is oriented  $38^\circ$  east of north (Colavita et al. 2004). The components of  $(\mathbf{B}/\lambda)$  projected on the sky are the spatial frequencies  $u$  and  $v$  commonly used in interferometry. The Earth’s rotation presents continually varying projections of the baseline with respect to the target and the interferometer measures  $V^2$  varying with  $u$  and  $v$ , or equivalently, time. Analysis of the measured  $V^2(u, v)$  is accomplished by fitting a binary model to the data.

The observations of NTTS 045251+3016 were interspersed with those of unresolved calibrators; Table 2 lists the calibrator spectral types, V and K-band magnitudes, and adopted angular diameters. The diameters were obtained from the SearchCal software tool developed by the JMMC Working Group (Bonneau et al. 2006, 2011). The visibilities were calibrated using the wbcilib program distributed by NExScI. The uncertainties are estimated from the scatter in the interferometric scans obtained on the target and calibrators. When running wbcilib, we applied the ratio correction, to account for when the flux from the two telescopes of the interferometer is unbalanced, and the flux bias correction, to account for the visibility dependence on target brightness. We rejected visibility measurements when the ratio correction exceeded 1.5. Table 3 lists the time of

observations, central wavelength, calibrated visibilities, and their corresponding  $u$  and  $v$  coordinates.

Given the limited  $(u, v)$  coverage on the sky, we fit the orbit (see Sect. 3.2) directly to the visibilities rather than measuring the separation and position angle during each epoch separately. This allows us to use additional dynamical information from the spectroscopic, AO, and NRM measurements to help constrain the binary position during the KI epochs. This is critical for nights with only a single KI observation of NTTTS 045251+3016 and also useful for nights with multiple KI observations but with limited rotation of the baseline on the sky.

We encountered a few difficulties when fitting the KI visibilities. First, we were not able to get a reasonable fit for the data on UT 2006 Dec 08. Inspection of the observing log from that night revealed that the counts from both telescopes were lower than expected, windshake on Keck II was  $\sim 10$  times higher than on Keck I when pointing into the wind, and significant aberrations were present in the images obtained from the Keck II angle trackers. Additionally, the ratio correction between the two telescopes was much higher for observations of NTTTS 045251+3016 compared with other targets and calibrators during the night, and varied over the sequence on NTTTS 045251+3016. Because of these issues, we opted not to include the KI data from 2006 Dec 08 in the fit.

The second complication was during the KI epochs when the binary was widely separated. In 2002 and 2004, the components in NTTTS 045251+3016 were separated by 35 mas and 29 mas, respectively (based on the orbital parameters presented in Sect 3.2). With a K-band filter width of  $0.3 \mu\text{m}$ , the coherence length  $(\frac{\lambda^2}{\Delta\lambda})$  of the KI corresponds to  $\sim 38$  mas on the sky. Therefore, the width of the fringe envelope from each component in the binary becomes important, so we added a bandwidth smearing term to the visibilities (e.g., Bridle & Schwab 1999; Lachaume & Berger 2012). However, these epochs were

complicated by one additional factor. The field of view of the KI is set by the width of the single mode fibers used in the fringe tracker and corresponds to  $\sim 45$  mas in the K-band. Therefore, at wide separations, not all of the light from both components will get through. Using our AO images of NTTS 045251+3016 taken in the K-band on 2009 Oct 25, when the binary is separated by  $\sim 36$  mas (§2.2), we estimate that if the KI field of view is centered on the center of light, then we expect to lose 15% more light from the secondary as compared with the primary in an aperture of 45 mas. Additionally, the amount of flux lost from the companion would depend on the seeing and quality of the AO correction; this would effectively change the flux ratio between the components on those nights. If there were enough KI measurements on these nights to sample the binary visibility curve sufficiently, then we would be able to measure the effective flux ratio independently for each night. However, because there was only one observing block on NTTS 045251+3016 during each of the nights when the binary was widely separated, we opted not to use the KI data from 2002–2004 in our orbital fit because of our inability to determine the arbitrary scaling of the visibilities.

The KI visibilities included in the orbit fit (§3.2) are marked by an asterisk in the last column of Table 3. Figure 1 plots the  $V^2$  values for each of these nights. The largest number of KI measurements was obtained on 2005 Oct 25; this night samples the binary visibility curve well and adds valuable dynamical constraints on the orbit fit.

## 2.2. Adaptive Optics Imaging

We used NIRC2, the facility near IR camera (Wizinowich et al. 2000), to obtain adaptive optics (AO) images on four occasions (Table 1). The images were recorded in the narrow-field mode with a plate scale  $9.952 \pm 0.002$  mas per pixel and an orientation of  $0.252^\circ \pm 0.009^\circ$  east of north (Yelda et al. 2010). The PMS stars DN Tau and LkCa 19

served as point spread function (PSF) references; their separations from NTTS 045251+3016 are  $7.7^\circ$  and  $5.4^\circ$ , respectively. Neither PSF star is known to have companions (Leinert et al. 1993; Prato et al. 2008; Kraus et al. 2011) and, at the distance of the Taurus SFR, their diameters are unresolvable by the AO observations.

Table 4 gives AO imaging specifications of the NTTS 045251+3016 observations. The target was observed using a standard three-point image dither pattern with  $\sim 2''$  offset. Each image was comprised of 10 coadded frames, each frame with an exposure time of 0.18–1.5 s. The PSF reference star was observed immediately before or after the target using the same dither pattern and AO frame rate to minimize changes in the shape and structure of the PSF. We collected a total of 6–12 images on target and 3–12 images of the PSF calibrator during each night. Post-observing processing of the raw images, and subsequent analysis were the same as we described in Schaefer et al. (2012). The images were flatfielded using dark-subtracted, median-filtered dome flats. Pairs of dithered exposures were subtracted to remove the sky background.

Figure 2 shows the co-added images of NTTS 045251+3016 and the PSF reference stars. The NTTS 045251+3016 binary was reliably resolved in all the observations except on UT 2011 Oct 12. Observations using the non-redundant masking technique (next section) did resolve the binary on that date at a separation of  $\sim 16$  mas. Fitting the standard AO data from the same night we measured a separation of  $\sim 17$  mas at a consistent position angle; however, the uncertainties were about four times larger compared with the results obtained with the aperture mask. The Airy criterion for the diffraction limited resolution of a 10-m diameter telescope is 40 mas at  $1.6 \mu\text{m}$ . We are not confident that we can measure separations half this size reliably using conventional AO observations without a simultaneous PSF reference in the field of view. For observations that require a separate PSF reference, as in the case of NTTS 045251+3016, the time-variability of the



AO correction limits our ability to resolve binaries with separations significantly smaller than the diffraction limit.

For each night, we used the PSF reference star to construct models of the binary while searching through a grid of separations and flux ratios and selecting the solution where the  $\chi^2$  between the data and model reached a minimum. Uncertainties were determined by analyzing multiple images individually and computing the standard deviation. We applied the geometric distortion solution of Yelda et al. (2010). Table 5 lists the separation  $\rho$ , position angle  $PA$  measured east of north, and flux ratio  $r$  derived from our NIRC2 observations.

### 2.3. Non-Redundant Masking Interferometry without Tears

NIRC2 includes a 9-hole mask that can be positioned in the pupil plane for observations by non-redundant masking interferometry (NRM)<sup>1</sup>. The 9 apertures provide 36 independent and unique baselines. Two apertures at the ends of a baseline form a simple two-element interferometer and produce an interferogram on the detector array with fringe spacing  $\lambda/B$  where  $B$  designates the baseline length as in eqn. (1). According to the usual criterion that two objects are resolvable when the maximum of the fringe pattern of one falls on the first minimum of the other, a two-element interferometer achieves resolution  $\sim 0.5\lambda/B$ , better than twice that of a uniformly illuminated aperture of diameter  $B$ . The Fourier transform of the interferogram produces signal at two locations in the  $u, v$  plane because the two apertures defining the baseline are indistinguishable. In actuality, the signal is spread over a small patch in the  $u, v$  plane, the result of convolution with the finite aperture

---

<sup>1</sup> The technique is also known as sparse aperture imaging. P. Tuthill’s layout for the apertures is given at the NIRC2 website: [www2.keck.hawaii.edu/inst/nirc2/specs.html](http://www2.keck.hawaii.edu/inst/nirc2/specs.html)

size. Lloyd et al. (2006) call these distributions of signal “splodges” (see their Figure 3); the term is so evocative and apt that we adopt it here. The amplitude squared of this Fourier transform, the power spectrum of the splodges, is the  $V^2$  of eqn (1). The phase, defined as  $\tan^{-1}(Im/Re)$ , where  $Im$  and  $Re$  are the imaginary and real parts of the Fourier transform, completes the structural information of the target. In contrast to the KI which may be considered a two-aperture synthesis interferometer, an NRM-equipped camera when operating on an equatorial mount telescope produces a stationary signal pattern in the  $u, v$  plane. Because Keck II is an elevation-azimuth mounted telescope the pattern produced on NIRC2’s detector array rotates during the observation.

The 36 baselines produce 36 interferograms superposed on the detector array. The two-dimensional Fourier transform of the signal recorded on the array produces 72 splodges in the  $u, v$  plane. The phase of the 2-D transform not only carries the structural information of the target, but also includes unavoidable phase errors induced by the atmosphere, incomplete wave-front correction, and systemics in the camera and processing. These errors cancel in forming the closure phase, the sum of the splodge phases around a triangle formed by 3 apertures (Baldwin et al. 1986; Nakajima et al. 1989; Tuthill et al. 2000). The splodges produced by the 9 apertures yield 84 closure phases, the number of combinations of 9 apertures taken 3 at a time. Closure phases measured on the target are calibrated by observations of a nearby unresolved star. When the target is a simple binary, the calibrated closure phases are then fit to a model to determine its  $\rho$ , PA, and  $r$  (e.g., Lloyd et al. 2006; Martinache et al. 2009; Kraus et al. 2011.)

We made all the NRM observations in the H-band, taking a series of dithered integrations on NTTS 045251+3016 followed by a series on LkCa 19. The numbers of integrations in each observation are given in Table 4. After dark-subtracting and flat-fielding the data as for other NIRC2 images, we calculated the closure phases for target and

calibrator using procedures written at Stony Brook. Differencing these yielded calibrated closure phases for NTT 045251+3016. We determined the best fitting binary parameters by minimizing the  $\chi^2$  of a model with respect to the data. In actual practice, the modeling routine requires two instrumental parameters: the rotation of the mask with respect to the detector array of the camera and the scale of the calculated Fourier transform of the interferogram with respect to the observed splodges. We determined these by identifying the correspondence of splodge locations of the calibrator with the Fourier transform of the interferogram of the unrotated mask. We checked the image scale and rotation by observing DF Tau, a  $\sim 100$  mas separation PMS binary, with both AO imaging and NRM on UT 2013 Jan 27; these results will be reported separately (Schaefer et al. 2013, in prep). The analysis also requires a telescope parameter, the orientation of the camera with respect to the sky. This changes as the altitude-azimuth mounted telescope tracks a star. It is calculated by the Keck facility software and provided in the image headers.

We analyzed the integrations of each observing session in groups of eight. Over the total time required for each group, the sky rotation was smaller than  $1.6^\circ$ . For each of the UT 2011 Jan 24 (Figure 3, *top*) and 2011 Oct 12 (Figure 3, *bottom*) sessions, we show the averaged closure phases for the first 8 integrations as a function of the longest baseline in the triangle for which a closure phase is measured. The best fit parameters in Table 5 are for the full data sets and the uncertainties are calculated from the analyses of the four groups of 8 integrations. The NRM-derived results for UT 2011 Jan 24 are in good agreement with those obtained with conventional AO-assisted imaging. On UT 2011 Oct 12, NRM resolved the binary components at separation  $\sim 16$  mas, demonstrating that it is possible to reach angular resolution as small as 40% of that given by the Airy criterion. If the binary were unresolved, all the closure phases would be zero. That the closure phases are smaller on the longest baselines in the October, 2011 observation than in the January, 2011 observation is a result of the smaller separation in October. At secondary/primary flux ratio  $\sim 0.4$  in the

H-band, our observations did not stress the contrast limits of the NRM technique; however, Kraus et al. (2011) showed that it is possible to reach 15:1 contrast in K-band observations of a large sample of stars in the Taurus-Auriga SFR.

Table 5 also includes our best fit parameters to the UT 2008 Dec 23 NRM data obtained and analyzed by Kraus et al. (2011)<sup>2</sup>. We analyzed the data independently because we wanted another check on our analysis procedures and because we wanted to use parameters derived uniformly for the orbital fit (§3). The separation, position angle and component flux ratio we derived for this observation are entirely consistent with Kraus et al.’s values except that the position angle uncertainty is larger.

#### 2.4. High Resolution IR Spectroscopy

We measured the RVs, rotational broadening, and determined the best matching spectral type for the primary and secondary using high-resolution, near-IR spectra taken with NIRSPEC on the Keck II telescope (McLean et al. 2000). Our observations were centered at  $\sim 1.555\mu\text{m}$  (order 49); the  $0.''288$  (2-pixel) wide slit provided spectral resolution 30,000. These observations did not use AO. As the component spectra were angularly unresolved, we used the 2-D cross-correlation procedure developed at Lowell Observatory (e.g., Mace et al. 2012) to recover the RVs of the two binary components. The best solution for the spectra was found with a K5V primary (HR 8085) and an M0V secondary (GL 763), corresponding to  $T_{\text{eff}} = 4415$  K and 3845 K (Luhman et al. 2003), respectively, each rotationally broadened to  $13 \text{ km s}^{-1}$ . The RV measurements are listed in Table 6. In Figure 4 these values are shown together with the visible light and IR measurements previously

---

<sup>2</sup>We obtained these data from the archives maintained at the *NASA Exoplanet Science Institute* (NExSci).

reported by Steffen et al. (2001).

### 3. Results and Discussion

#### 3.1. Spatially Resolved Binary Separations

Figure 5 shows our AO and NRM astrometric measurements and the computed location of the binary during the times of the KI observations; the orbit was fit directly to the KI visibilities (§2.1). The parameters of our orbital fit are reported in Table 7 and discussed in the following section. Figure 5 also shows the earlier FGS measurements of Steffen et al. (2001); clearly their and our new measurements are discrepant. We suspect a fault in the FGS results because the new measurements appear consistent with each other and were derived by three different techniques.

The FGS is sensitive in the visible and operates as a scanning interferometer along two orthogonal axes. Using the separation and position angle measurements reported by Steffen et al. (2001) and the spacecraft roll angle during each observation, we derived the separations along the FGS ( $X, Y$ ) axes that they must have measured. Of the 28 individual ( $X, Y$ ) values for their 14 reported positions, 18 are smaller than 20 mas, with 5 under 10 mas. It has been our experience that it is not possible to get a meaningful fit to an FGS transfer function with  $\Delta V \gtrsim 2$  mag (as reported by Steffen et al.) at such small separations.

We downloaded the FGS data on NTTS 045251+3016 from the *HST* archive and attempted to fit the scans with two different templates, SAO 185689 and HD 233877. The magnitude differences and separations we derived varied widely for the epochs with small separations. Interestingly, we obtained similar fits along the  $Y$  axis for the epochs with larger separations (30–40 mas). Based on these results, we suspect that the source of the discrepancy in the astrometric measurements lies in the difficulty of detecting a faint

component ( $\Delta V \gtrsim 2$  mag) when the separation is small along one of the axes of the FGS.

### 3.2. Orbital Parameters, Masses, and Distance

The full ensemble of RV data (Figure 4) uniquely determines  $K_1$  and  $K_2$ , the velocity semi-amplitudes of the primary and secondary, and hence their mass ratio. The visual orbit (Figure 5) uniquely determines the apparent semi-major axis  $a$ , in angular measure, and the orbital inclination  $i$ . Either the orbital RVs or the visual orbit, or both together, determine the orbital period  $P$ , time of periastron passage  $T$ , eccentricity  $e$ , and longitude of the periastron,  $\omega$ . Together, the visual and spectroscopic orbits determine the masses of the primary and secondary,  $M_1$  and  $M_2$ , semi-major axis,  $a$ , and the distance to NTTS 045251+3016 (e.g., Schaefer et al. 2008):

$$M_1 = \frac{1.036 \times 10^{-7} (K_1 + K_2) K_2 P (1 - e^2)^{\frac{3}{2}}}{\sin^3 i} \quad (2)$$

and likewise for  $M_2$ , with  $K_1$  replacing the second  $K_2$ . Also,

$$a \sin i = 0.01375 (K_1 + K_2) P (1 - e^2)^{\frac{1}{2}} \quad \text{and} \quad (3)$$

$$d = \frac{a(\text{AU})}{a('')}, \quad (4)$$

where the  $K$ 's are in km/s,  $P$  in days,  $M$  in solar units,  $a$  in  $10^6$  km (except in Eqn. 4, where  $a$  is given in AU and arcsec), and  $d$  is in pc.

We carried out a simultaneous orbit fit to the AO and NRM astrometric measurements, the interferometric visibilities, and the RVs using a Newton-Raphson technique to determine all ten orbital parameters including the center-of-mass velocity  $\gamma$ , and position angle of the nodes,  $\Omega$ . We also measured the K-band flux ratio from the KI visibilities during the fit. These values are given in Table 7.

To demonstrate how the different data sets help determine the orbit, we performed a  $\chi^2$  search for orbital solutions within the  $1\sigma$  ( $\Delta\chi^2 = 1$ ) and  $3\sigma$  ( $\Delta\chi^2 = 9$ ) confidence intervals. We randomly chose values for  $a$ ,  $i$ , and  $\Omega$  and optimized the fit for  $P$ ,  $T$ ,  $e$ ,  $\omega$ ,  $K_1$ ,  $K_2$ ,  $\gamma$ , and the flux ratio at K. Except for the flux ratio, the latter parameters are well-constrained by the RV measurements while the former are derived from the AO, NRM, and KI measurements. The  $1\sigma$  intervals obtained for each parameter from the  $\chi^2$  search agree well with the formal uncertainties determined from the covariance matrix (Table 7). In Figure 1, we show how the fit to the KI visibilities changes if we vary  $a$ ,  $i$ , and  $\Omega$  by their  $1$  and  $3\sigma$  uncertainties while optimizing the remaining parameters. The same range of orbits is plotted in the right panel of Figure 5 to show how they fit the AO and NRM measurements. Each orbit found through the  $\chi^2$  search gives a slightly different position of the companion during the times of the KI epochs. In the left panel of Figure 5 we overplot the  $\Delta\chi^2 = 1$  surfaces that define the  $1\sigma$  uncertainty ranges in  $\Delta\text{RA}$  and  $\Delta\text{DEC}$  (small blue ellipses inside the open circles).

Of the new parameters derived in Table 7, those determined by the orbital RVs are in reasonable agreement with the values reported by Steffen et al. (2001). Our addition of 8 new measurements of the secondary’s RV improves the reliability of its semi-amplitude,  $K_2$ , and hence of the mass ratio,  $q$ . Our new astrometric orbit affects the semi-major axis in angular measure,  $a''$ , and inclination,  $i$ , and hence the derived masses and distances (e.g., eqns. 3-4). Compared to Steffen et al.’s values,  $a''$  decreases from  $\sim 32$  to  $26$  mas, and  $i$  changes from  $\sim 114^\circ$  to  $\sim 78^\circ$ . As a result, the masses of the components decrease,  $M_1$  from  $1.45 M_\odot$  to  $0.86 M_\odot$  and  $M_2$  from  $0.81 M_\odot$  to  $0.55 M_\odot$ . The precisions of the new mass determinations,  $0.86 \pm 0.11$  and  $0.55 \pm 0.05 M_\odot$  are hardly improved from the precisions of Steffen et al.’s values, mostly because we could not extract meaningful results from the FGS data. We compare the new mass values with theoretical calculations of PMS calculations in the following section.

The new values of semi-major axis and inclination increase the distance of NTTS 045251+3016 to  $\sim 158.7 \pm 3.9$  pc with respect to Steffen et al.’s value,  $\sim 144.8 \pm 8.3$  pc. NTTS+045251+3016 thus lies on the far-side of the SFR with respect to a mean distance estimate of 140 pc (Kenyon et al. 1994). This is consistent with the spread of distances determined using the VLBA (Torres et al. 2009), but is inconsistent with Bertout & Genova’s (2006) estimate,  $116_{-12}^{+14}$ , probably because their determination used an early value of the center-of-mass velocity quoted from Walter et al. (1988) in the Herbig and Bell Catalog (Herbig & Bell 1988).

### 3.3. Comparison with Evolutionary Tracks

We compare the measured masses with the evolutionary tracks of Baraffe et al. (1998, BCAH), Siess et al. (2000, SDF), Tognelli et al. (2011, Pisa) and the Dartmouth group (Feiden et al. 2011 and references therein; Dartmouth). To place the components of NTTS 045251+3016 on Hertzsprung-Russell diagrams (HRDs) requires their effective temperatures,  $T_{\text{eff}}$ , and luminosities,  $L$ . For the primary, we use  $T_{\text{eff}} = 4345_{-138}^{+194}$  K derived by Steffen et al. (2001) from consideration of visible light spectra. This is within 70 K of the temperature corresponding to the K5 spectral type determined on the basis of the IR spectra and converted to  $T_{\text{eff}}$  using the results in Luhman et al. (2003; §2.4). We use Steffen et al.’s  $T_{\text{eff}}$  because the uncertainties are smaller and because the 70 K difference in results between the two is negligible. For the secondary we estimated  $T_{\text{eff}} = 3845_{-130}^{+200}$  (Luhman et al.), corresponding to its M0 spectral type and  $\pm$  one subclass uncertainty.

For the BCAH, SDF, and Dartmouth tracks it is convenient to plot the absolute magnitudes of the components at H or K as proxies for the luminosity. To calculate these we used the total apparent 2-MASS magnitudes at H and K, apportioned the flux to the primary and secondary according to the average of the flux ratios given in Table 5, and



applied the distance modulus  $6.00 \pm 0.05$  mag corresponding to the distance  $158.7 \pm 3.9$  pc (Table 7). We applied no correction for extinction because Walter et al.’s (1988) photometry of NTTS 045251+3016 indicates that its extinction at K is negligible. The Pisa tracks are presented in terms of luminosity. We calculated luminosities of the components from their  $M_K$  values by applying the bolometric correction and (V-K) color appropriate to their  $T_{\text{eff}}$  as given by Kenyon & Hartmann (1995). Component luminosities using their  $M_H$  values are consistent. The uncertainties of the absolute magnitudes and luminosity include uncertainties in photometry, average flux ratios, and distance propagated in quadrature.

Figure 6 shows the primary and secondary plotted on the BCAH, SDF, Pisa, and Dartmouth evolutionary tracks for ages between 1 and 10 Myr. We plot the BCAH tracks for mixing length parameter  $\alpha = 1.0$  below  $0.6 M_{\odot}$ , and  $\alpha = 1.9$  for greater masses. The SDF tracks use  $\alpha = 1.605$  and the Pisa tracks are available for two values of  $\alpha$ , 1.20 and 1.68; we show both. The Dartmouth tracks use  $\alpha = 1.83$  (Dotter et al. 2008). We consider two questions:

- 1) Are the evolutionary tracks consistent with the measured masses?
  
- 2) What is the age of NTTS 045251+3016?

The answers are mostly limited by the uncertainties of the primary and secondary’s masses and  $T_{\text{eff}}$ . The effects of uncertainties in luminosity or absolute magnitude are smaller because the evolutionary tracks are nearly parallel to the abscissa at the ages we consider. Table 8 summarizes the range of masses and ages derived from the tracks.

We consider first the primary with measured mass  $0.86 \pm 0.11 M_{\odot}$ . On the HRD for

the Pisa models (Figure 6c) the primary star falls close to the  $1.0 M_{\odot}$  evolutionary track for the  $\alpha = 1.68$  model and is consistent with lower mass tracks corresponding to its measured dynamical mass. The primary’s location on the BCAH, SDF, and Dartmouth tracks is consistent to a similar extent with its measured mass as well. The evolutionary codes adjust the mixing length parameter to fit the parameters of the Sun. Evidently this yields models that satisfy PMS stars of mass close to  $1 M_{\odot}$ . On all the HRDs, the  $T_{\text{eff}}$  uncertainty spans about  $\pm 0.1 M_{\odot}$ , about the same as the uncertainty in the mass. Improvement in both uncertainties to at least half the present values would allow a more discriminating assessment of agreement with the tracks. The age of the primary is within  $3 \pm 2$  Myr on all the HRDs.

The secondary star, with mass  $0.55 \pm 0.05 M_{\odot}$ , is close to agreement with the Pisa tracks for the  $\alpha = 1.20$  models and similarly with the BCAH, SDF, and Dartmouth models. The effective temperature is the biggest limitation preventing a closer assessment of agreement with the tracks. There is a considerable spread in ages indicated,  $\sim 3$  to nearly 10 Myr. There is no reason to suppose that the components are not coeval. Improvement in the  $T_{\text{eff}}$  estimate is necessary to resolve this discrepancy. The age of the secondary star is consistent with a coeval age of 3 Myr for all save the BCAH tracks, although it generally spans a slightly older age range than the primary; on the BCAH tracks it appears to be 5–9 Myr.

These comparisons of the derived parameters of the primary and secondary with the HRDs indicate that effective temperatures better than  $\pm 100^{\circ}$  K and mass precisions better than  $\pm 10\%$  are required to discriminate among the models more definitively than possible at present. The latter can be accomplished by an improvement of the astrometric orbit. This requires only time and patience. We have started a project to improve the effective temperature determinations by a comparison of high resolution spectra of the stars

with synthetic spectra following an approach similar to that of Rice et al. (2010) applied to brown dwarfs. For main sequence stars of spectral type late G to early M we reach  $T_{eff}$  uncertainties of  $\pm 50\text{K}$  and will explore whether this accuracy can be achieved for the more active atmospheres of PMS stars.

#### 4. Summary

On the basis of our analysis of data taken at the Keck II telescope using the interferometer, adaptive optics imaging, adaptive optics “interferometry” with non-redundant masking, and high resolution IR spectroscopy of the NTTS 045251+3016 binary, we present the following summary and conclusions:

- 1) We have determined the NTTS 045251+3016 orbital parameters as a resolved visual binary and double-lined spectroscopic binary.
- 2) The masses of the primary and secondary stars are  $0.86 \pm 0.11$  and  $0.55 \pm 0.05 M_{\odot}$ , respectively.
- 3) The distance to the system is  $158.7 \pm 3.9$  pc, placing it on the far side of the Taurus-Auriga SFR.
- 4) The measured masses and distance differ significantly from the values determined by Steffen et al. (2001). Their orbit is in error possibly because their astrometry with the FGS on the HST relied on measurements from the FGS at the limits of its sensitivity.
- 5) By determining the primary and secondary star absolute H or K magnitude or luminosity and  $T_{eff}$  and plotting their locations on HRDs, we compare the evolutionary tracks calculated by Baraffe et al. (1998), Siess et al. (2000), Tognelli et al. (2011), and the Dartmouth group (Feiden et al. 2011). We find that these tracks are mostly consistent within the uncertainties compared to the measured dynamical mass of the primary and

indicate an age  $\sim 3$  Myr. The secondary star dynamical mass is least consistent with the BCAH tracks. It appears older than 3 Myr on all the tracks but, given the uncertainties in  $T_{\text{eff}}$ , it would be premature to believe that the components are not coeval.

6) Improvement in comparisons of empirical data for stars of mass less than  $\sim 1 M_{\odot}$  with the several theoretical calculations of evolution to the main sequence will require precisions on the mass of better than  $\pm 10\%$ , and  $\pm 100$  K on  $T_{\text{eff}}$ .

MS thanks Anand Sivaramakrishnan for advice concerning analysis of NRM data and Peter Tuthill for information about the implementation of NRM at Keck. We thank C. Beichman for the opportunity to obtain an additional NIRSPEC spectrum on the night of UT 2010 Nov 22. We are grateful to Rachel Akeson helpful discussions on analyzing and interpreting the KI data. We thank the staff at Keck Observatory for their superb support during and after our use of the several instruments. Data presented herein were obtained at the W. M. Keck Observatory from telescope time allocated to the National Aeronautics and Space Administration through the agency’s scientific partnership with the California Institute of Technology and the University of California. Keck telescope time was also granted by NOAO, through the Telescope System Instrumentation Program (TSIP). TSIP is funded by NSF. The Observatory was made possible by the generous financial support of the W. M. Keck Foundation. We recognize the Hawaiian community for the opportunity to conduct these observations from the summit of Mauna Kea. The Keck Interferometer was funded by the National Aeronautics and Space Administration (NASA) as part of its Exoplanet Exploration program. This work has made use of software produced by the NASA Exoplanet Science Institute (NExSci) at the California Institute of Technology. This research has also made use of the Keck Observatory Archive (KOA), which is operated by the W. M. Keck Observatory and NExSci, under contract with the NASA. Our work was supported in part by NSF Grants AST-09-08406 (MS) and AST-1009136 (LP). GHS

acknowledges support from NASA Keck PI Data Award administered by NExSci (JPL contract 1441975).

## REFERENCES

- Baraffe, I., Chabrier, G., Allard, F., & Hauschildt, P. H. 1998, *A&A*, 337, 403 (BCAH)
- Baldwin, J. E., Haniff, C. A., Mackay, C. D., & Warner, P. J. 1986, *Nature*, 320, 595
- Berger, J. P., & Segransan, D. 2007, *New A Rev.*, 51, 576
- Bertout, C., & Genova, F. 2006, *A&A*, 460, 499
- Boden, A. F. 2000, in *Principles of Long Baseline Stellar Interferometry*, ed. P. R. Lawson (Pasadena, CA: JPL), 9, <http://olbin.jpl.nasa.gov/iss1999/coursenotes.html>
- Bonneau, D., Clausse, J.-M., Delfosse, X., et al. 2006, *A&A*, 456, 789
- Bonneau, D., Delfosse, X., Mourard, D., et al. 2011, *A&A*, 535, A53
- Bridle, A. H., & Schwab, F. R. 1999, *Synthesis Imaging in Radio Astronomy II*, 180, 371
- Colavita, M. M., Wizinowich, P. L., & Akeson, R. L. 2004, *Proc. SPIE*, 5491, 454
- Cutri, R. M., Skrutskie, M. F., van Dyk, S., et al. 2003, *VizieR Online Data Catalog*, 2246, 0
- Dotter, A., Chaboyer, B., Jevremović, D., et al. 2008, *ApJS*, 178, 89
- Feiden, G. A., Chaboyer, B., & Dotter, A. 2011, *ApJ*, 740, L25
- Herbig, G. H., & Bell, K. R. 1988, *Third catalog of emission-line stars of the Orion population.*, by G.H. gerbig and K.R. Bell. *Lick Observatory Bulletin #1111*, Santa Cruz: Lick Observatory, June 1988, 90
- Hillenbrand, L. A., & White, R. J. 2004, *ApJ*, 604, 741
- Kenyon, S. J., Dobrzycka, D., & Hartmann, L. 1994, *AJ*, 108, 1872

- Kenyon, S. J., & Hartmann, L. 1995, *ApJS*, 101, 117
- Kharchenko, N. V., & Roeser, S. 2009, *VizieR Online Data Catalog*, 1280, 0
- Kraus, A. L., Ireland, M. J., Martinache, F., & Hillenbrand, L. A. 2011, *ApJ*, 731, 8
- Lachaume, R., & Berger, J.-P. 2012, *Proc. SPIE*, 8445, 3
- Leinert, C., Zinnecker, H., Weitzel, N., et al. 1993, *A&A*, 278, 129
- Lloyd, J. P., Martinache, F., Ireland, M. J., et al. 2006, *ApJ*, 650, L131
- Luhman, K. L., Briceño, C., Stauffer, J. R., et al. 2003, *ApJ*, 590, 348
- Mace, G. N., Prato, L., Torres, G., et al. 2012, *AJ*, 144, 55
- Martinache, F., Rojas-Ayala, B., Ireland, M. J., Lloyd, J. P., & Tuthill, P. G. 2009, *ApJ*, 695, 1183
- McLean, I. S., Graham, J. R., Becklin, E. E., et al. 2000, *Proc. SPIE*, 4008, 1048
- Nakajima, T., Kulkarni, S. R., Gorham, P. W., et al. 1989, *AJ*, 97, 1510
- Rice, E. L., Barman, T., Mclean, I. S., Prato, L., & Kirkpatrick, J. D. 2010, *ApJS*, 186, 63
- Schaefer, G. H., Simon, M., Prato, L., & Barman, T. 2008, *AJ*, 135, 1659
- Schaefer, G. H., Prato, L., Simon, M., & Zavala, R. T. 2012, *ApJ*, 756, 120
- Siess, L., Dufour, E., & Forestini, M. 2000, *A&A*, 358, 593
- Simon, M., Dutrey, A., & Guilloteau, S. 2000, *ApJ*, 545, 1034
- Simon, M. 2008, *The Power of Optical/IR Interferometry: Recent Scientific Results and 2nd Generation*, 227

Steffen, A. T., Mathieu, R. D., Lattanzi, M. G., et al. 2001, *AJ*, 122, 997

Tognelli, E., Prada Moroni, P. G., & Degl’Innocenti, S. 2011, *A&A*, 533, A109

Torres, R. M., Loinard, L., Mioduszewski, A. J., & Rodríguez, L. F. 2009, *ApJ*, 698, 242

Tuthill, P. G., Monnier, J. D., Danchi, W. C., Wishnow, E. H., & Haniff, C. A. 2000, *PASP*,  
112, 555

Walter, F. M., Brown, A., Mathieu, R. D., Myers, P. C., & Vrba, F. J. 1988, *AJ*, 96, 297

Wizinowich, P. L., Acton, D. S., Lai, O., et al. 2000, *Proc. SPIE*, 4007, 2

Wizinowich, P. L., Akeson, R. L., Colavita, M. M., et al. 2004, *Proc. SPIE*, 5491, 1678

Yelda, S., Lu, J. R., Ghez, A. M., et al. 2010, *ApJ*, 725, 331



Table 1. Log of Observations

UT Date	Instrument	Filter	Calibrators/PSF Stars
2002 Oct 24	Keck Interferometer	K	HD 27741, 27777, 29645
2002 Nov 21	Keck Interferometer	K	HD 27777
2004 Jan 09	Keck Interferometer	K	HD 27741, 27777, 35076
2005 Oct 25	Keck Interferometer	K	HD 27741, 29645
2006 Nov 11	Keck Interferometer	K	HD 27741, 27282
2006 Dec 08	Keck Interferometer	K	HD 27741, 27282
2007 Oct 28	Keck Interferometer	K	HD 27741
2008 Dec 17	NIRC2+AO	Hcont, Kcont	DN Tau
2009 Oct 25	NIRC2+AO	Hcont, Kcont	DN Tau
2011 Jan 24	NIRC2+AO	Hcont	LkCa 19
2011 Oct 12	NIRC2+AO	Hcont	LkCa 19
2011 Jan 24	NIRC2+AO+NRM	H	LkCa 19
2011 Oct 12	NIRC2+AO+NRM	H	LkCa 19
2001 Jan 05	NIRSPEC	1.55 $\mu$ m	
2001 Dec 31	NIRSPEC	1.55 $\mu$ m	
2002 Feb 05	NIRSPEC	1.55 $\mu$ m	
2004 Dec 26	NIRSPEC	1.55 $\mu$ m	
2006 Dec 07	NIRSPEC	1.55 $\mu$ m	
2006 Dec 14	NIRSPEC	1.55 $\mu$ m	
2009 Dec 06	NIRSPEC	1.55 $\mu$ m	
2010 Nov 22	NIRSPEC	1.55 $\mu$ m	

Table 2. Adopted Angular Diameters of KI Calibrators

Calibrator Name	Spectral Type	V (mag)	K (mag)	Diameter (mas)
HD 27282	G8V	8.5	6.8	$0.199 \pm 0.014$
HD 27741	G0V	8.3	6.8	$0.196 \pm 0.014$
HD 27777	B8V	5.7	5.8	$0.172 \pm 0.012$
HD 29645	G0V	6.0	4.6	$0.533 \pm 0.037$
HD 35076	B9V	6.4	6.5	$0.127 \pm 0.009$

Note. — Spectral types and V magnitudes from Kharchenko & Roeser (2009), K magnitudes from 2MASS (Cutri et al. 2003), angular diameters from SearchCal (Bonneau et al. 2006, 2011).

Table 3. KI  $V^2$  Measurements

MJD	UT Date	UTC	$u$ (m)	$v$ (m)	$\lambda$ ( $\mu\text{m}$ )	$V^2$	$\sigma_{V^2}$	Fit
52571.52737	2002 Oct 24	12:39:24	54.086	63.082	2.18	0.658	0.037	
52571.52956	2002 Oct 24	12:42:33	53.854	63.458	2.18	0.605	0.043	
52599.52655	2002 Nov 21	12:38:13	40.508	74.691	2.18	0.712	0.063	
52599.52824	2002 Nov 21	12:40:39	40.086	74.908	2.18	0.758	0.062	
53013.38074	2004 Jan 09	09:08:15	43.537	72.987	2.18	0.655	0.089	
53668.56213	2005 Oct 25	13:29:27	48.617	69.341	2.15	0.567	0.036	*
53668.56353	2005 Oct 25	13:31:28	48.361	69.557	2.15	0.560	0.026	*
53668.59009	2005 Oct 25	14:09:43	42.806	73.422	2.15	0.400	0.019	*
53668.59141	2005 Oct 25	14:11:37	42.497	73.601	2.15	0.384	0.021	*
53668.60165	2005 Oct 25	14:26:22	40.004	74.948	2.15	0.335	0.023	*
53668.60296	2005 Oct 25	14:28:15	39.674	75.113	2.15	0.329	0.024	*
53668.61347	2005 Oct 25	14:43:23	36.922	76.395	2.15	0.257	0.019	*
53668.61526	2005 Oct 25	14:45:58	36.437	76.604	2.15	0.249	0.020	*
53668.61974	2005 Oct 25	14:52:25	35.200	77.116	2.15	0.255	0.021	*
53668.62150	2005 Oct 25	14:54:57	34.708	77.312	2.15	0.250	0.021	*
54050.56118	2006 Nov 11	13:28:06	38.664	75.604	2.18	0.537	0.044	*
54077.46703	2006 Dec 08	11:12:31	43.644	72.922	2.18	0.521	0.041	
54077.51305	2006 Dec 08	12:18:47	31.546	78.471	2.18	0.786	0.087	
54401.63071	2007 Oct 28	15:08:13	30.045	78.963	2.18	0.605	0.107	*
54401.63225	2007 Oct 28	15:10:26	29.579	79.109	2.18	0.630	0.113	*

Note. — An asterisk in the last column indicates that the measurement was included in the orbit fit.

Table 4. Log of NIRC2+AO Observations

UT Date	Target	UTC	Mode	Filter	AO Rate	$T_{\text{int}}(\text{s})$	Co-adds	Images
2008 Dec 17	NTTS 045251+3016	09:03	AO	Kcont	250	1.5	10	12
	NTTS 045251+3016	09:11	AO	Hcont	250	1.2	10	12
	DN Tau	09:24	AO	Hcont	250	0.3	10	6
	DN Tau	09:26	AO	Hcont	250	1.0	10	6
	DN Tau	09:31	AO	Kcont	250	1.0	10	12
2009 Oct 25	NTTS 045251+3016	15:36	AO	Kcont	438	0.5	10	6
	NTTS 045251+3016	15:40	AO	Hcont	438	0.5	10	6
	DN Tau	15:44	AO	Hcont	438	0.2	10	3
	DN Tau	15:47	AO	Kcont	438	0.2	10	3
2011 Jan 24	LkCa 19	08:57	AO	Hcont	438	0.3	10	6
	NTTS 045251+3016	09:01	AO	Hcont	438	0.3	10	12
	NTTS 045251+3016	09:20	AO+NRM	H	438	20.0	1	16
	LkCa 19	09:35	AO+NRM	H	438	20.0	1	16
	NTTS 045251+3016	09:53	AO+NRM	H	438	15.0	1	16
	LkCa 19	10:05	AO+NRM	H	438	15.0	1	16
2011 Oct 12	NTTS 045251+3016	14:12	AO	Hcont	438	0.5	10	12
	NTTS 045251+3016	14:18	AO	Kcont	438	0.5	10	12
	LkCa 19	14:23	AO	Hcont	438	0.5	10	6
	LkCa 19	14:28	AO	Kcont	438	0.5	10	6
	NTTS 045251+3016	14:48	AO+NRM	H	438	5.0	1	16
	LkCa19	14:53	AO+NRM	H	438	5.0	1	8
	LkCa19	14:57	AO+NRM	H	438	4.0	1	8
	NTTS 045251+3016	15:05	AO+NRM	H	438	4.0	1	16
	LkCa19	15:11	AO+NRM	H	438	4.0	1	16

Table 5. Astrometric Results

UT Date	MJD	Instrument	$\rho(\text{mas})$	PA(deg)	Flux Ratio
2008 Dec 17	54817.383	NIRC2+AO	$33.0 \pm 1.3$	$175.4 \pm 2.3$	$0.385 \pm 0.032$ (K), $0.418 \pm 0.037$ (H)
2009 Oct 25	55129.653	NIRC2+AO	$35.9 \pm 2.5$	$179.8 \pm 4.1$	$0.408 \pm 0.036$ (K), $0.488 \pm 0.037$ (H)
2011 Jan 24	55585.375	NIRC2+AO	$27.6 \pm 3.8$	$182.4 \pm 7.9$	$0.445 \pm 0.103$ (H)
2008 Dec 23 <sup>a</sup>	54823.528	NIRC2+AO+NRM	$32.2 \pm 0.1$	$180.8 \pm 1.8$	$0.41 \pm 0.01$ (K)
2011 Jan 24	55585.412	NIRC2+AO+NRM	$27.4 \pm 0.3$	$186.2 \pm 2.7$	$0.44 \pm 0.01$ (H)
2011 Oct 12	55846.617	NIRC2+AO+NRM	$16.2 \pm 1.4$	$194.9 \pm 2.5$	$0.27 \pm 0.02$ (H)

<sup>a</sup>Analysis of NRM data published by Kraus et al. (2011); see text for discussion.

Table 6. Radial Velocities of the Primary and Secondary

MJD	UT Date	$V_1$ km s <sup>-1</sup>	$\sigma_1$ km s <sup>-1</sup>	$V_2$ km s <sup>-1</sup>	$\sigma_2$ km s <sup>-1</sup>	Phase
51914.311	2001.012	14.68	1.00	14.80	2.00	0.102
52274.344	2001.998	18.85	1.00	7.34	2.00	0.244
52310.313	2002.097	18.90	1.00	6.50	2.00	0.258
53365.428	2004.985	16.14	1.00	13.50	2.00	0.674
54076.537	2006.933	4.39	1.00	31.69	2.00	0.954
54083.025	2006.953	2.70	1.00	29.42	2.0	0.957
55171.395	2009.930	18.48	1.00	7.60	2.00	0.385
55522.592	2010.892	17.64	1.00	11.65	2.00	0.523

Table 7. Orbital Parameters, Masses, and Distance

Parameter	Value
$P$ (days)	$2513.8 \pm 2.9$
$T$ (MJD)	$51626.3 \pm 9.9$
$e$	$0.4937 \pm 0.0071$
$a$ (mas)	$25.57 \pm 0.12$
$i$ ( $^\circ$ )	$78.1 \pm 1.0$
$\Omega$ ( $^\circ$ )	$178.06 \pm 0.77$
$\omega$ ( $^\circ$ )	$213.0 \pm 1.7$
$K_1$ (km/s)	$7.67 \pm 0.14$
$K_2$ (km/s)	$12.09 \pm 0.44$
$\gamma$ (km/s)	$14.43 \pm 0.09$
KI flux ratio at $K$	$0.389 \pm 0.042$
$M_1$ ( $M_\odot$ )	$0.86 \pm 0.11$
$M_2$ ( $M_\odot$ )	$0.55 \pm 0.05$
$q = M_2/M_1$	$0.635 \pm 0.026$
$d$ (pc)	$158.7 \pm 3.9$
$\chi^2$	98.7
$\chi^2_\nu$	1.05

Table 8. Comparison of Dynamical and Track Masses

Source	$M_1$ ( $M_\odot$ )	Age (Myr)	$M_2$ ( $M_\odot$ )	Age (Myr)
This Work	$0.86 \pm 0.11$	...	$0.55 \pm 0.05$	...
Baraffe et al. (1998)	$1.05^{+0.20}_{-0.10}$	$3 \pm 1$	$0.70^{+0.15}_{-0.05}$	$8 \pm 3$
Siess et al. (2000)	$1.10^{+0.15}_{-0.20}$	$3 \pm 2$	$0.60^{+0.20}_{-0.10}$	$4 \pm 3$
Tognelli et al. (2011)	$0.95 \pm 0.15^a$	$3 \pm 2^a$	$0.70^{+0.20}_{-0.10}^b$	$5 \pm 3^b$
Feiden et al. (2011)	$1.00 \pm 0.15$	$3 \pm 1$	$0.65^{+0.20}_{-0.10}$	$5 \pm 3$

<sup>a</sup>Mixing length parameter = 1.68.

<sup>b</sup>Mixing length parameter = 1.20.

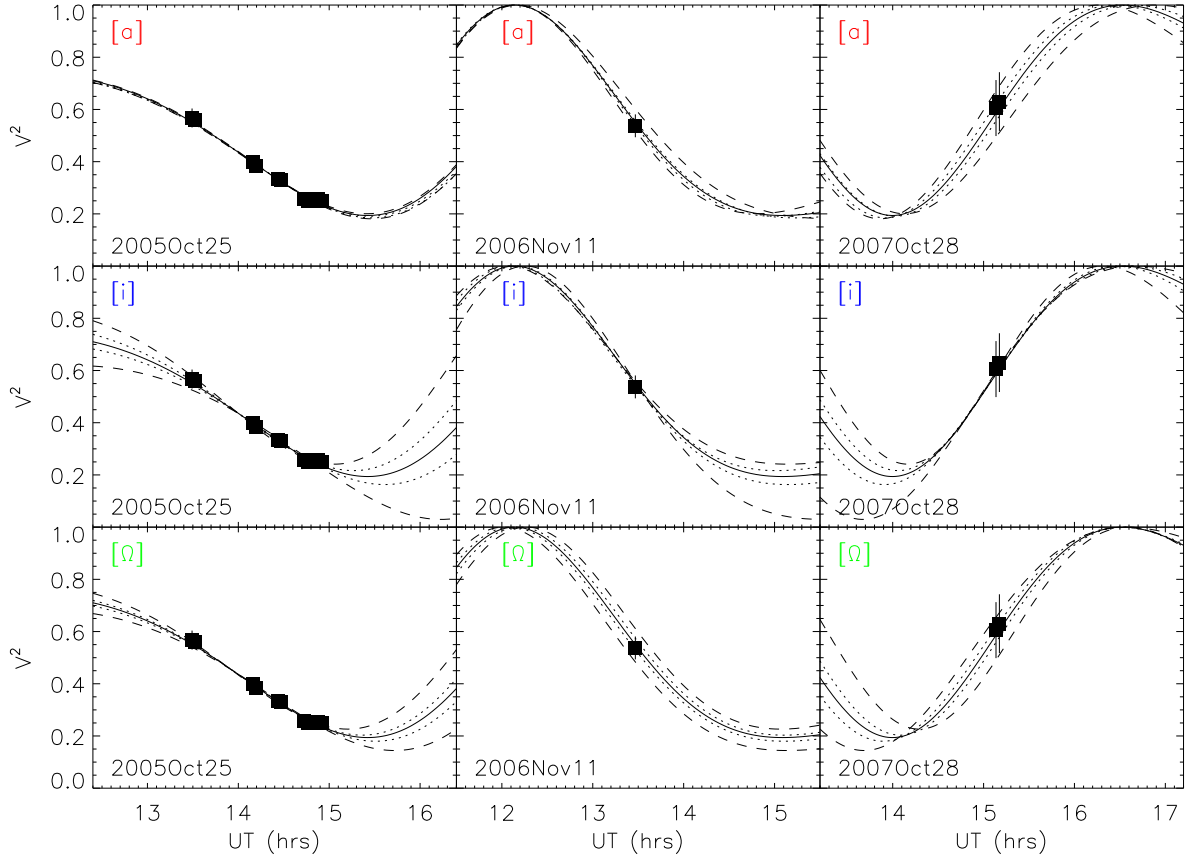


Fig. 1.— Calibrated visibilities measured with the Keck Interferometer on UT 2005 October 25, 2006 November 11, and 2007 October 28. The solid lines shows the simultaneous orbit fit to the RV, AO, NRM, and KI data. In each panel, we show how the fit changes if we vary the semi-major axis (top row), inclination (middle row), and  $\Omega$  (bottom row) by their  $1\sigma$  (dotted line) and  $3\sigma$  (dashed line) uncertainties while optimizing the remaining parameters. The parameter being varied is identified in brackets in the top left corner of each plot. The dashed orbits that represent the  $3\sigma$  intervals for  $a$ ,  $i$ , and  $\Omega$  are also plotted in Figure 5 to show how they compare with the AO and NRM measurements.

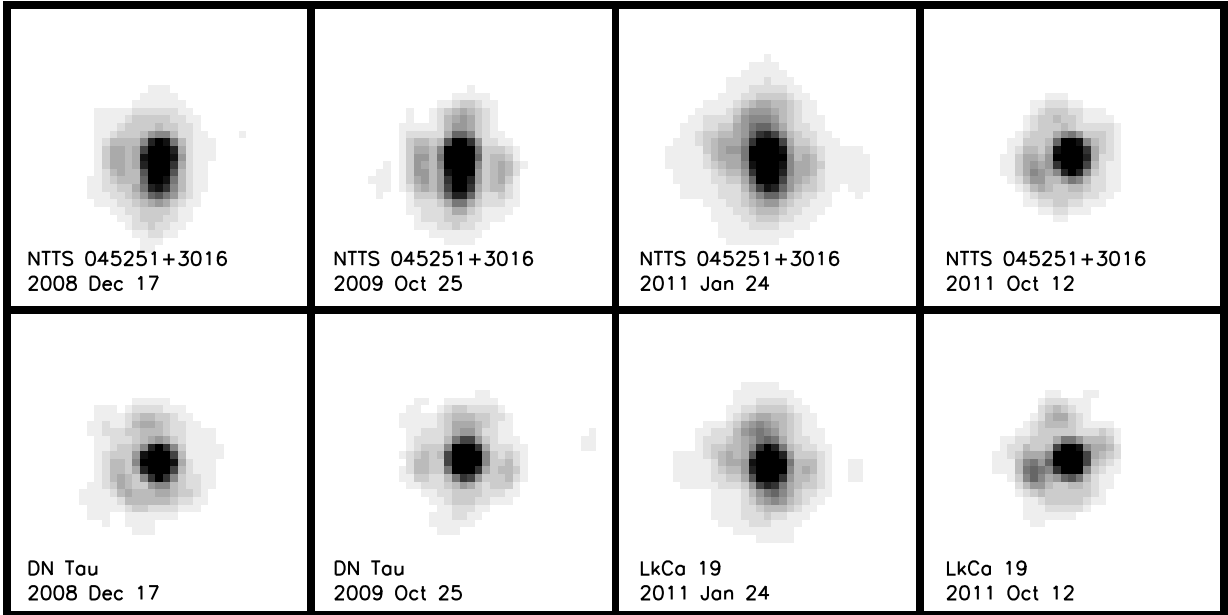


Fig. 2.— H-band images of NTTS 045251+3016 (top) and the point-spread function (PSF) calibrators DN Tau and LkCa 19 (bottom) obtained with NIRC2 operating with Adaptive Optics on UT 2008 Dec 17, 2009 Oct 25, 2011 Jan 24, and 2011 Oct 12. The AO images of NTTS 0455251+3016 in 2008, 2009, and Jan 2011 resolved the binary but those taken in Oct 2011 when NRM observations revealed that the separation was  $\sim 16$  mas (Table 4) did not reliably resolve the pair. Each panel is 400 mas wide.



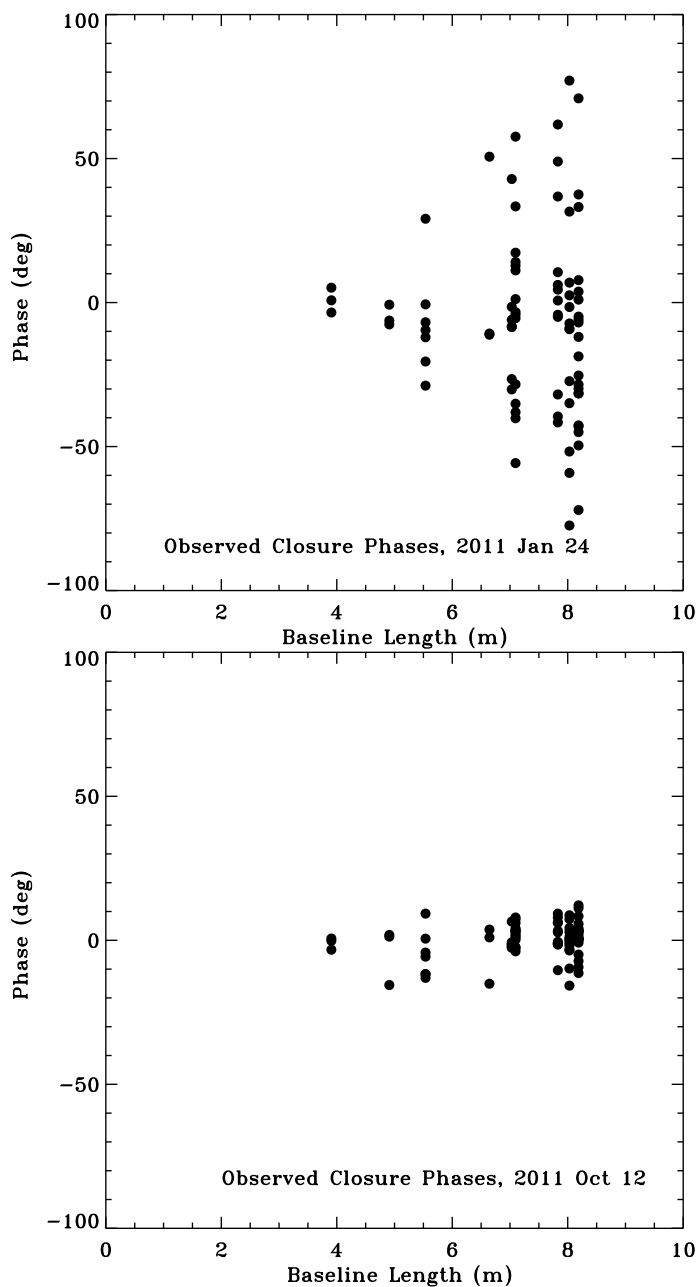


Fig. 3.— Closure phase (degrees) *vs* longest baseline (meters) in the triangle for which it is measured for NRM data obtained on UT 2011 Jan 24 (*top*) and 2011 Oct 12 (*below*). For each data set, average closure phases are shown only for the first quarter of each data set (see text). The binary separation, position angle, and flux ratio of the models that fit each data set best are reported in Table 4.

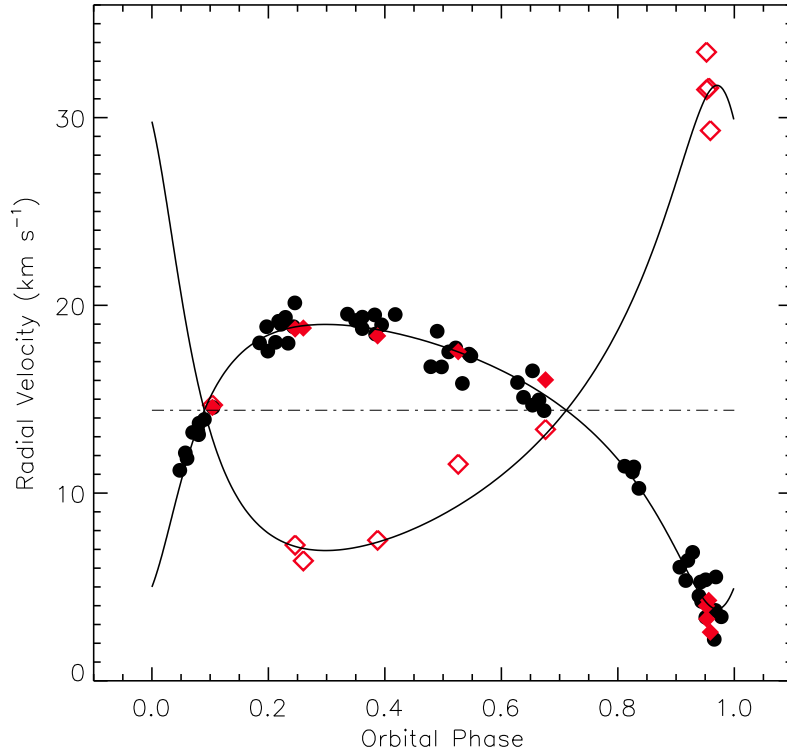


Fig. 4.— RV as a function of phase for the primary (filled symbols) and secondary (open symbols) stars in NTTS 04251+3016. The black circles represent Steffen et al.’s (2001) measurements of the primary RV in visible light. The red symbols were measured in IR light. K5V and M0V spectral templates were used to measure the RVs derived from the IR spectra (§2.4). The two IR measurements at phase 0.953 and 9.954 were reported previously by Steffen et al.

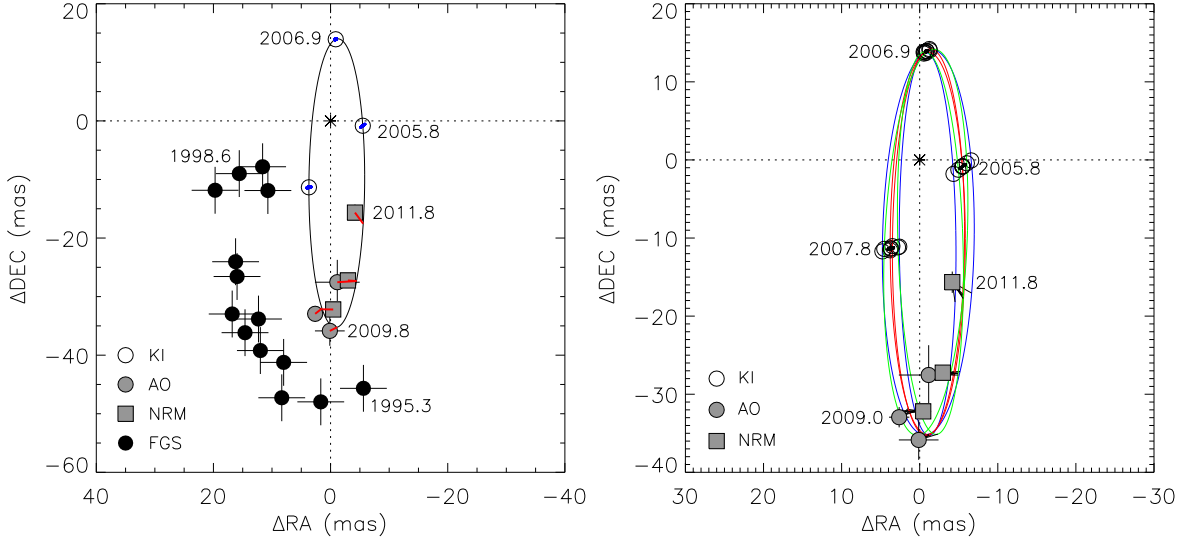


Fig. 5.— *Left:* Visual orbit of NTTS 04251+3016 based on the fit to the AO, NRM, KI, and RV measurements. The shaded grey circles indicate the AO data and the shaded grey squares represent the NRM measurements. The red lines connect the measured values with the computed positions from the orbit fit. The computed positions of the binary during the epochs of the KI observations are marked by the open circles. The small blue ellipses within the open circles show the variation in  $\Delta\text{RA}$  and  $\Delta\text{DEC}$  during the times of the KI epochs that are generated by exploring the range of orbital solutions that fit the data within the  $1\sigma$  ( $\Delta\chi^2 = 1$ ) confidence interval. The figure also includes the FGS measurements (black circles) reported by Steffen et al. (2001). They are obviously inconsistent with the new observations reported here. We discuss the possible reason for the discrepancy in §3.1. *Right:* Range of orbits obtained by varying  $a$  (red),  $i$  (blue), and  $\Omega$  (green) by their  $3\sigma$  uncertainties while optimizing the remaining parameters. These are the same orbits that are plotted as dashed lines in Figure 1 and illustrate how varying the orbital parameters affects simultaneously the fits to the KI visibilities and the AO/NRM measurements. The computed position of the binary during the epochs of the KI observations (open circles) varies depending on the orbital parameters.

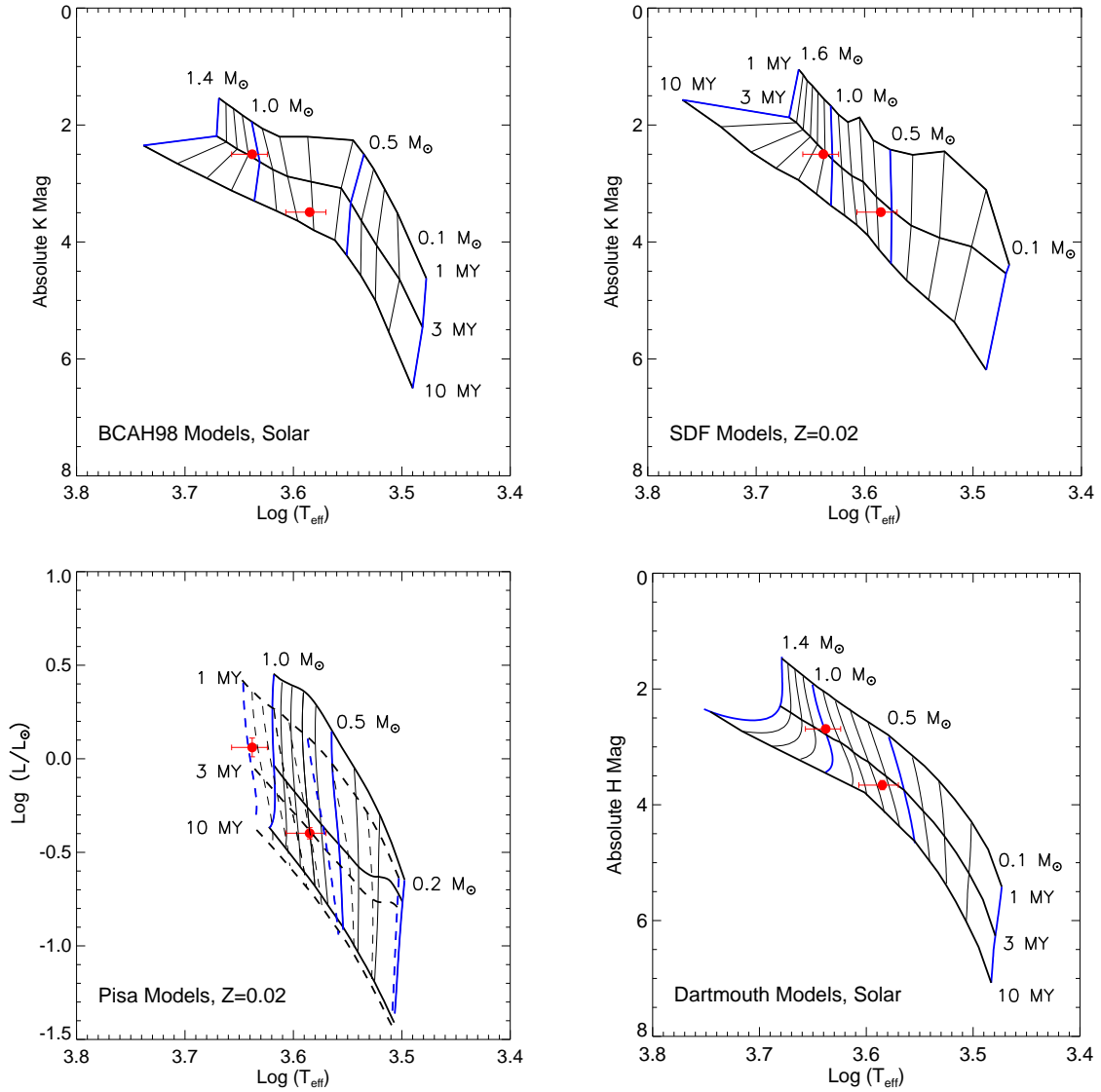


Fig. 6.— HRDs showing the location of the primary and secondary in NTTS 045251+3016 with respect to theoretical PMS evolutionary tracks and isochrones. The vertical uncertainties include those in photometry, flux ratio, and distance (see §3.3). *Top left:* Evolutionary tracks of BCAH at solar metallicity for masses of 0.1 to 1.4  $M_{\odot}$ . For masses below 0.6  $M_{\odot}$ , we used the tracks calculated with a mixing length parameter  $\alpha = 1.0$ ; for larger masses we used the tracks with  $\alpha = 1.9$ . This HRD uses the absolute K-band magnitude,  $M_K$ , as a proxy for the luminosity. *Top right:* Evolutionary tracks of SDF at  $Z = 0.02$  for masses of 0.1 to 1.6  $M_{\odot}$  again using  $M_K$ . *Bottom left:* Pisa stellar evolutionary models (Tognelli et al. 2011) for  $\alpha = 1.20$  (solid lines) and 1.68 (dashed lines) at a metallicity of  $Z = 0.02$ . *Bottom right:* The Dartmouth tracks at solar abundances and  $\alpha = 1.83$ , using  $M_H$  (Feiden et al. 2011). The isochrones are plotted for 1, 3, and 10 Myr. Labelled mass tracks are plotted in blue. Uncertainties in the y-axes are on the order of or smaller than the plot symbols.